



## Evaluating Gilbert damping in magnetic insulators from first-principles

Liangliang Hong, Changsong Xu, and Hongjun Xiang \*

Key Laboratory of Computational Physical Sciences (Ministry of Education), Institute of Computational Physical Sciences, State Key Laboratory of Surface Physics, and Department of Physics, Fudan University, Shanghai 200433, China and Shanghai Qi Zhi Institute, Shanghai 200030, China

 (Received 10 September 2023; revised 7 February 2024; accepted 23 February 2024; published 20 March 2024)

Magnetic damping poses a significant impact on the performance of various magnetic and spintronic devices, making it a longstanding focus of research. The strength of magnetic damping is usually quantified by the Gilbert damping constants in the Landau-Lifshitz-Gilbert equation. Here we propose a first-principles-based approach to evaluate the damping constant contributed by spin-lattice coupling in magnetic insulators. The approach involves effective Hamiltonian models and spin-lattice dynamics simulations. As a case study, we applied our method to  $\text{Y}_3\text{Fe}_5\text{O}_{12}$ ,  $\text{MnFe}_2\text{O}_4$ , and  $\text{Cr}_2\text{O}_3$ . Their damping constants were calculated to be  $0.8 \times 10^{-4}$ ,  $0.2 \times 10^{-4}$ ,  $2.2 \times 10^{-4}$ , respectively at a low temperature. The results for  $\text{Y}_3\text{Fe}_5\text{O}_{12}$  and  $\text{Cr}_2\text{O}_3$  are very close to the experimental results, while the large discrepancy in  $\text{MnFe}_2\text{O}_4$  can be attributed to the inhomogeneity and small band gap in real samples. The stronger damping observed in  $\text{Cr}_2\text{O}_3$ , compared to  $\text{Y}_3\text{Fe}_5\text{O}_{12}$ , essentially results from its stronger spin-lattice coupling. In addition, we confirmed a proportional relationship between damping constants and the temperature difference of subsystems, which had been reported in previous studies. These successful applications suggest that our approach can be a viable candidate for estimating the Gilbert damping constant in magnetic insulators.

DOI: [10.1103/PhysRevB.109.094429](https://doi.org/10.1103/PhysRevB.109.094429)

### I. INTRODUCTION

Recent decades have witnessed rapid developments in magnetism and spintronics [1–3]. A long-time pursuit in spintronics is to actively control and manipulate the spin degrees of freedom in solid-state systems. Related fundamental studies involve spin transport, spin dynamics, and spin relaxation [4]. Within these domains, magnetic damping often plays a crucial role. Generally, stronger damping enables a faster writing rate for magnetic memories, while lower damping leads to a longer propagation distance of spin waves. Therefore, it is always essential to accurately evaluate the magnetic damping in different materials and further understand the intrinsic mechanisms behind. For instance, yttrium iron garnet (YIG) is a highly promising spintronic material due to its ultra-low magnetic damping [5–7]. Although some theoretical studies have made efforts to investigate the mechanism responsible for its unique property [8], this issue has still yet to be fully elucidated, which partly motivated us to carry out this study.

At present, magnetic damping is typically represented by a phenomenological term in the well-known Landau-Lifshitz-Gilbert (LLG) equation [9], which is widely employed to simulate magnetization dynamics. A general form of the equation can be written as [10]

$$\frac{\partial \mathbf{m}_i}{\partial t} = \mathbf{m}_i \times \left( -\gamma \mathbf{B}_i^{\text{eff}} + \sum_j \frac{\alpha_{ij}}{|\mathbf{m}_j|} \frac{\partial \mathbf{m}_j}{\partial t} \right), \quad (1)$$

where  $\mathbf{B}_i^{\text{eff}}$  represents the effective magnetic field acting on the local dipole  $\mathbf{m}_i$ ,  $\gamma$  is the gyromagnetic ratio, and  $\alpha_{ij}$  denotes a nonlocal Gilbert damping tensor [11–14]. In this paper, we would like to adopt a simplified form of the LLG equation,

$$\frac{\partial \mathbf{m}_i}{\partial t} = -\gamma \mathbf{m}_i \times \mathbf{B}_i^{\text{eff}} + \frac{\alpha}{|\mathbf{m}_i|} \mathbf{m}_i \times \frac{\partial \mathbf{m}_i}{\partial t}, \quad (2)$$

which is more commonly utilized in the practical simulations [15]. The difference between two equations is that the anisotropy and nonlocal effects of magnetic damping are neglected in the latter one, where  $\alpha$  becomes a scalar damping constant. The simplified form could be a reasonable approximation in our paper for the following reasons. Firstly, some previous studies on the transition-metal ferromagnets have shown that the nonlocal damping is much smaller than the on-site contribution [10,13]. Secondly, the anisotropy of magnetic damping have been demonstrated related to the presence of interface/surface effects and local structural distortions [16], which are beyond the scope of our study. Thirdly, the magnetic ions considered in our study are all sited in the center of oxygen octahedrons or tetrahedrons. Assuming that the local damping matrix is mainly determined by the nearby environment and the structural distortion from standard polyhedrons is small, it can be derived from symmetry analyses that the damping matrix must be diagonal with equal elements.

The second term on the right-hand side of LLG equation, as we mentioned, directly leads to the relaxation process, in which the energy dissipation rate is totally determined by the Gilbert damping constant. Given the importance of  $\alpha$  in magnetization dynamics, its origin has been extensively

\*hxiang@fudan.edu.cn

studied in the literature [17–20]. To our best knowledge, the macroscopic Gilbert damping contains intrinsic and extrinsic contributions, the former of which mainly originates from spin-lattice and spin-electron couplings, and the latter mostly involves lattice imperfections [21–23]. In magnetic metals, the intrinsic damping primarily relies on the spin-electron coupling and electron-hole recombination that dissipates energy to the lattice. Another well-known damping process is two-magnon scattering, which falls into the category of extrinsic mechanisms [24–26]. As one type of non-Gilbert relaxation, two-magnon scattering does not transfer energy from the spin subsystem to the other degrees of freedom in the studied system. Compared to the above two sources of magnetic damping, spin-lattice coupling has not received much attention due to its much smaller contribution in metallic systems. However, spin-lattice interaction becomes one of the major contributors of damping in magnetic insulators, where electronic effects are reduced due to the presence of a finite band gap. In this paper, we focus on the estimation of damping constants in insulating magnets, and we think our results will be useful for simulating the propagation of magnons.

Two types of first-principles-based methods have been developed to calculate the damping constants in the past. One approach involves the breathing Fermi surface model [27,28] and the torque correlation model [29,30], while the other is based on the scattering theory from linear response [11,31,32]. These methods have demonstrated remarkable success in studying the magnetic damping in transition metals such as Fe, Co, and Ni. Despite being free from complicated experiments, these theoretical approaches still exhibit several limitations. Firstly, when dealing with complex systems, we often have to spend a significant amount of computing resources on the first-principles calculations. In addition, these methods are more suitable for calculating the electronic contribution to Gilbert damping in metallic magnets, thus rarely taking the effects of spin-lattice coupling into consideration [21,33].

Recently, spin-lattice dynamics (SLD) simulations [34] have been utilized as an alternative method to estimate the Gilbert damping parameters. In Ref. [33], the authors constructed an empirically parameterized Hamiltonian model for a cobalt cluster. They coupled a preheated lattice with a fully ordered spin state, then performed SLD simulation. During the relaxation process, the energy of lattice and spin subsystems were recorded and fitted to the following logistic functions:

$$U_{\text{lat}} = U_0^{\text{lat}} - \frac{\Delta U_0}{1 + \exp[-\eta \Delta U_0 t - \Theta]}, \quad (3)$$

$$U_{\text{mag}} = U_0^{\text{mag}} + \frac{\Delta U_0}{1 + \exp[-\eta \Delta U_0 t - \Theta]}, \quad (4)$$

from which they extracted the relaxation rate  $\Gamma = \eta \Delta U_0$  and calculated the damping constant  $\alpha = \eta \mu_S / \gamma$ . Here,  $\mu_S$  denotes the magnitude of magnetic moments. In Ref. [35], the authors also built an empirical potential model for a periodic bcc Fe system. They firstly applied an external magnetic field in the  $z$  direction and thermalized the system to a finite temperature. Then, the magnetization orientation of each atom was rotated artificially by a same angle. Afterwards, the system would relax back to equilibrium, during which the

averaged  $z$  component of atomic magnetization was recorded and fitted to the following function:

$$m_z(t) = \tanh \left[ \frac{\alpha}{1 + \alpha^2} \gamma B_{\text{ext}}(t + t_0) \right], \quad (5)$$

where  $\alpha$  was exactly the Gilbert damping parameter to be estimated. Since these studies selected transition metals as the research object, their results were both orders of magnitude smaller than the experimental values. In addition, the use of empirically parameterized models reduced the reliability of their simulated results.

In this paper, we combine SLD simulations with first-principles-based effective Hamiltonian models to evaluate the damping constants in magnetic insulators, where the dominant contribution results from spin-lattice couplings. Compared to the previous studies, our study has made improvements mainly in two aspects. Firstly, the utilization of first-principles-based Hamiltonian models in simulations enhances the accuracy of our conclusions. Besides, the better choice of research objects allows for demonstrating the superiority of SLD simulations. In particular, the microscopic origin of low damping in YIG will be investigated. The paper is organized as follows. In Sec. II, we introduce our effective Hamiltonian model, parametrization methods, and a scheme for estimating Gilbert damping parameters. Then, both the validation and application of our method are presented in Sec. III. Finally, we summarize this paper and present a brief outlook in Sec. IV.

## II. MODEL AND METHODS

This section is split into three parts. Firstly (in Sec. II A), we introduce a generic form of our effective Hamiltonian model. Then, methods involving the calculation of model parameters are presented in Sec. II B. In the last part (Sec. II C), we propose a scheme to determine the Gilbert damping constant through dynamics simulations.

### A. The Hamiltonian model

Since our purpose is to evaluate the contribution of spin-lattice coupling to magnetic damping, the effective Hamiltonian model must incorporate both spin and lattice degrees of freedom. A concise and generic formula that meets our basic requirements consists of the three terms as follows:

$$H = H_L(\{u_{i,\alpha}\}) + H_S(\{s_j\}) + H_{SL}(\{u_{i,\alpha}, s_j\}), \quad (6)$$

where  $\alpha$  abbreviates three orthogonal axes,  $u_{i,\alpha}$  represents the displacement of atom  $i$ , and  $s_j$  is a unit vector that represents the direction of spin  $j$ .

The first term  $H_L$  in Hamiltonian model describes the dynamical behavior of individual phonons. Technically, we take the atomic displacements as independent variables and expand the Hamiltonian to the second order with Taylor series. Then, we have the form as

$$H_L = \frac{1}{2} \sum_{ij} \sum_{\alpha\beta} K_{ij,\alpha\beta} u_{i,\alpha} u_{j,\beta} + \frac{1}{2} \sum_{i,\alpha} M_i \dot{u}_{i,\alpha}^2, \quad (7)$$

where  $K_{ij,\alpha\beta}$  denotes the force constant tensor and  $M_i$  represents the mass of atom  $i$ .

Similarly, the second term  $H_S$  describes the dynamical behavior of individual magnons. For simplicity but no loss of accuracy, we only considered the Heisenberg exchange interactions between neighboring magnetic ions here, although more complex interactions could have been taken into account in principle. Therefore, this term can be expressed as

$$H_S = \sum_{(i,j)} J_{ij} \mathbf{S}_i \cdot \mathbf{S}_j, \quad (8)$$

where  $J_{ij}$  denotes the Heisenberg exchange coefficient.

The third term  $H_{SL}$  represents the coupling between spin and lattice subsystems, and is expected to describe the scattering process between phonons and magnons. As an approximation of the lowest order, this term can be written as

$$H_{SL} = \sum_{(i,j)} \sum_{k,\alpha} \left( \frac{\partial J_{ij}}{\partial u_{k,\alpha}} u_{k,\alpha} \right) \mathbf{S}_i \cdot \mathbf{S}_j. \quad (9)$$

According to the theory of quantum mechanics, this coupling term provides a fundamental description of the single-phonon scattering process, which is also adopted by the effective field theory (EFT) technique [36,37]. In history, the contribution of this mechanism to ferromagnetic resonance (FMR) linewidth was theoretically studied by Kasuya and LeCraw for the first time [38]. We note that some important terms, namely the single-ion anisotropy (SIA) and the Dzyaloshinskii-Moriya interactions (DMI), which originate from the spin-orbit coupling (SOC) effects, are not present here. These terms provide channels for angular momentum transfer between spin and lattice subsystems [39,40], but later we will show that taking these terms into consideration only leads to a small increase in the estimated damping constants. Also, higher orders of Taylor expansion with respect to atomic displacements could have been included to improve the accuracy of our Hamiltonian models. For example, the scattering between individual phonons can be described by anharmonic terms, and the change of phonon spectra due to magnon variations can be included by adding fourth order terms. As one always has to make a trade-off between the precision and complexity of models, in this paper we choose to neglect these higher-order terms since these interactions do not play a significant role in our concerned issues.

In this study, we adopted the symmetry-adapted cluster expansion method implemented in the Property Analysis and Simulation Package for Materials (PASP) [41] to build the Hamiltonian model presented above. This package can identify the nonequivalent interactions and equivalent atom clusters in a crystal system by analyzing its structural properties based on the group theory. A significant benefit of working with PASP is we are enabled to describe the target system with the least number of parameters. In the next section, we will discuss how to calculate the model parameters.

## B. Calculation of model parameters

Firstly, the Heisenberg exchange coefficients  $J_{ij}$  and spin-lattice coupling constants  $\partial J_{ij} / \partial u_{k,\alpha}$  can be calculated with the four-state method [42–51]. The basic flow is to construct four artificially designated spin states of the target system, calculate the corresponding energies and forces based on the

density functional theory (DFT), then determine the parameters by proper combination of those results. At the last step, the following formulas will be used:

$$J_{ij} = \frac{E^{\uparrow\uparrow} + E^{\downarrow\downarrow} - E^{\uparrow\downarrow} - E^{\downarrow\uparrow}}{4S^2}, \quad (10)$$

$$\frac{\partial J_{ij}}{\partial u_{k,\alpha}} = \frac{F_{k,\alpha}^{\uparrow\uparrow} + F_{k,\alpha}^{\downarrow\downarrow} - F_{k,\alpha}^{\uparrow\downarrow} - F_{k,\alpha}^{\downarrow\uparrow}}{4S^2}, \quad (11)$$

where  $S$  is the spin quantum number of magnetic atoms,  $E$  is the total energy of system, and  $F_{k,\alpha}$  refers to one component of the force on atom  $k$ . The superscripts ( $\uparrow\uparrow$ ,  $\downarrow\downarrow$ ,  $\uparrow\downarrow$ ,  $\downarrow\uparrow$ ) specify the constrained spin states of system in the calculation. More technical information about the four-state method can be found in Refs. [42,43].

Compared with the TB2J technique [52], which is also a widely used approach for extracting exchange parameters, the four-state method is simpler both theoretically and practically. Generally, the exchange parameters calculated by TB2J technique are more suitable for describing the low-energy excitation of magnetic systems, while the parameters obtained by four-state method are applicable in a larger temperature region at a relative loss of precision. For many magnetic systems, these two methods give similar results [53].

Since atomic masses  $M_i$  can be directly obtained from the periodic table, more efforts are needed to deal with the force constant tensor  $K_{ij,\alpha\beta}$ . Currently, there are two commonly adopted ways to calculate the force constant tensor: density functional perturbation theory (DFPT) and finite displacement method. Both of these methods are applicable to our task.

However, we cannot directly use the force constant tensor obtained from first-principles calculations as model parameters. The reason is that in dynamics simulations we usually expand crystal cells to reduce the undesired influence of thermal fluctuations, but calculating the force constant tensor for such a large supercell is not feasible. One common approach is to set a cutoff radius for each atomic site, and disregard the out-of-range interactions. In practice, we would calculate the force constant tensor in a small cell, extract the needed elements as model parameters, then expand the cell and perform simulations. However, a problem related to translational symmetry occurs in the above steps, since our operation equals to artificially setting some of the elements to zero, and this will make the force constant tensor violate the so called acoustic summation rules,

$$\sum_i K_{ij,\alpha\beta} = 0 \quad \text{for all } j, \alpha, \beta. \quad (12)$$

Note that a straightforward enforcement of the acoustic summation rules, achieved by subtracting errors uniformly from the force constants, will break the inherent crystal symmetries, which is the technique employed in phonopy [54]. To address the above issue, we adopted a more appropriate method in this paper. Recall that due to the crystal symmetries not each element of the force constant tensor serves as an independent variable. Taking the cubic cell of  $\text{Y}_3\text{Fe}_5\text{O}_{12}$  (containing 160 atoms), for example, there are totally 230 400 elements in the tensor. After symmetry analyses, we find that only 597 independent variables  $\{p_n\}$  are needed to adequately determine all the tensor elements  $\{K_{ij,\alpha\beta}(\{p_n\})\}$ , where the

effect of cutoff radius (11.0 Bohr) is already considered. Our method is to set a correction factor  $x_n$  for each variable  $p_n$  and minimize the deviation of parameters under the constraints of Eq. (12). A mathematical reformulation of this method can be written as

$$\min_{\{x_n\}} \sum_n (x_n - 1)^2, \text{ with} \quad (13)$$

$$\sum_i K_{i,j,\alpha\beta}(\{x_n p_n\}) = 0 \quad \text{for all } j, \alpha, \beta.$$

For the case of  $\text{Y}_3\text{Fe}_5\text{O}_{12}$ , there are 1440 constraints defined in Eq. (13), from which we could extract 18 linearly independent constraints. Then, the extremum problem is solved rigorously and the obtained correction factors are used to modify the force constants. The modified force constant tensor restores positive definiteness and translational symmetry while maintaining the crystal symmetries. Finally, the model parameters meet our requirements and can be used in dynamics simulations. In Sec. III B, this method will be further illustrated through a specific example.

For simplicity, we did not use the nonanalytical term correction [55,56] to explicitly consider the long-range dipole-dipole interaction, despite the presence of polar modes in our studied compounds. It will be shown later that in the simulated relaxation process the lattice only acts as a heat reservoir bridging the spin system and the external environment. Hence, the spin-lattice coupling constants contribute primarily to the estimated damping parameters, while a relatively rough treatment of lattice motion does not impact the results significantly. We may consider to improve our treatment of force constants in polar materials in the future work.

All the first-principles calculations mentioned in this section are carried out using the Vienna *Ab Initio* Simulation Package (VASP) [57–59]. The force constants and phonon spectra are obtained by phonopy [54]. The optimizations formulated in Eq. (13) are accomplished with the function `optimize.minimize` implemented in SciPy [60].

### C. Evaluation of damping constants

After the construction and parametrization of Hamiltonian models, we are finally able to perform spin-lattice dynamics simulations. Before the evaluation of Gilbert damping constants, we briefly introduce the framework of SLD to cover some relevant concepts. In practice, the motion of magnetic moments follows the stochastic Landau-Lifshitz-Gilbert (LLG) equation [21],

$$\frac{d\mathbf{m}_i}{dt} = -\gamma_L \mathbf{m}_i \times (\mathbf{B}_i + \mathbf{B}_i^{\text{fl}}) - \gamma_L \alpha \frac{\mathbf{m}_i}{|\mathbf{m}_i|} \times [\mathbf{m}_i \times (\mathbf{B}_i + \mathbf{B}_i^{\text{fl}})], \quad (14)$$

where  $\gamma_L$  is the renormalized gyromagnetic ratio,  $\mathbf{B}_i = -\partial H / \partial \mathbf{m}_i$  is the effective local magnetic field, and  $\mathbf{B}_i^{\text{fl}}$  refers to a stochastic field introduced by Langevin thermostat. At the same time, the motion of atoms obeys the Newton's equation,

$$\frac{d\dot{u}_{i,\alpha}}{dt} = \frac{1}{M_i} (F_{i,\alpha} + F_{i,\alpha}^{\text{fl}}) - \nu \dot{u}_{i,\alpha}, \quad (15)$$

where  $\nu$  is the damping constant and  $F_{i,\alpha}^{\text{fl}}$  refers to a stochastic force caused by thermal fluctuations. In this paper,  $\mathbf{B}_i^{\text{fl}}$  and  $F_{i,\alpha}^{\text{fl}}$  are modeled as normally distributed noises with temperature-dependent variances,

$$\mathbf{B}_{i,\beta}^{\text{fl}} \sim N(0, \sqrt{2\alpha k_B T_S / \gamma |\mathbf{m}_i| \delta t}), \quad (16)$$

$$F_{i,\beta}^{\text{fl}} \sim N(0, \sqrt{2\nu M_i k_B T_L / \delta t}), \quad (17)$$

where  $T_S$  and  $T_L$  refer to the equilibrium temperature of spin and lattice subsystems respectively. During simulations, we can also measure the transient temperature of each subsystem with the following formulas [61]:

$$T_S = \frac{\sum_i |\mathbf{m}_i \times \mathbf{B}_i|^2}{2k_B \sum_i \mathbf{m}_i \cdot \mathbf{B}_i}, \quad T_L = \frac{1}{3k_B N} \sum_{i,\alpha} M_i \dot{u}_{i,\alpha}^2. \quad (18)$$

In this paper, the LLG equation is numerically solved with the semi-implicit SIB method proposed by Mentink *et al.* [62]. The Newton's motion equation is integrated using the Grønbech-Jensen-Farago Verlet-type method [63]. To ensure the stability of those algorithms, a step length of 0.5 or 0.2 fs is adopted [64], where the shorter one is used in energy-conserving simulations.

Based on the combination of atomistic spin dynamics (ASD) and SLD simulations, a scheme is proposed to evaluate the damping constant in magnetic materials. Here is the basic flow of this method and more details of a specific application are presented in Sec. III B.

(1) Freeze the spin degree of freedom and thermalize the lattice from 0 to  $T_L$  in the simulation.

(2) Fix atomic positions and raise the temperature of spin to  $T_S > T_L$ . Compared to  $T_L > T_S$ , this type of nonequilibrium state is more common in actual scenarios and theoretical studies [65].

(3) Perform an energy-conserving SLD simulation to relax the system. Normally, the spin temperature will decrease to the same as lattice and stay there till the end.

(4) Conduct a series of ASD simulations with different Gilbert damping constants. The initial states are the same as in step 3 and the equilibrium temperatures are set to be  $T_L$ .

(5) Compare the cooling rates  $\partial T_S / \partial t$  of spin system between SLD and ASD simulations to evaluate the equivalent Gilbert damping constant contributed by spin-lattice coupling.

The motivation behind step 5 is that the cooling rates observed in ASD simulations are related to the assigned damping constants, while in SLD simulation the cooling rate is determined by the strength of spin-lattice coupling. Note that the former relation can be viewed as a natural result of the LLG equation, and a quantitative derivation is shown in Appendix.

Moreover, we would like to emphasize two points here. Firstly, the damping constant calculated from the above scheme is essentially an average value that contains the contribution of magnons with different wave vectors. By contrast, the measurements of magnetic damping in experiments are mostly based on the FMR technique, where only the damping of magnons with  $q = 0$  can be observed. Although it is inappropriate to directly compare our results with FMR experiments, the calculated damping parameter should be a more suitable choice for simulating the motion of spin waves with finite wave lengths. When we refer to



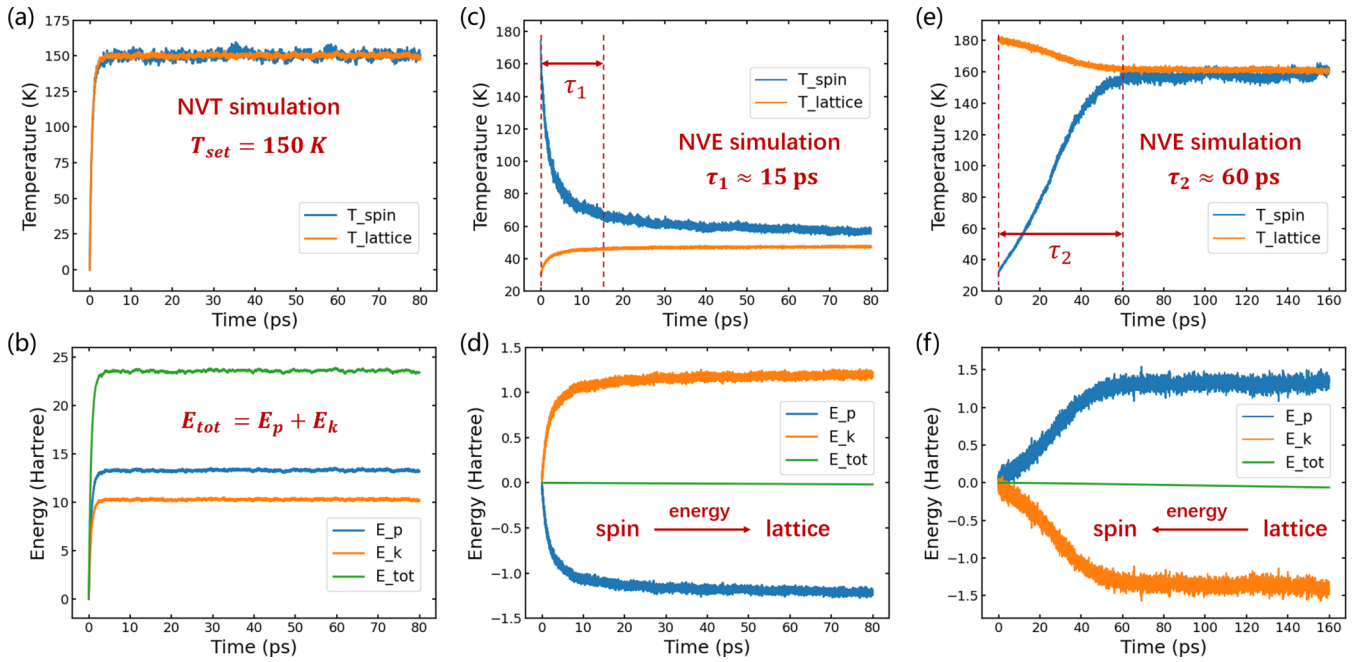


FIG. 1. NVT and NVE relaxations of a spin-lattice coupled system ( $\text{Cr}_2\text{O}_3$ ) within the framework of spin-lattice dynamics. The top row plots the time evolution of temperatures and the bottom row shows the variation of potential, kinetic and total energies. [(a),(b)] NVT thermalization from  $T_L = T_S = 0\text{ K}$  to  $T_L = T_S = 150\text{ K}$ . [(c),(d)] NVE relaxation with  $T_L = 30\text{ K}$ ,  $T_S = 175\text{ K}$  initially. [(e),(f)] NVE relaxation with  $T_L = 180\text{ K}$ ,  $T_S = 30\text{ K}$  initially.

experimental values later, we are not claiming that our results agree with experiments but only regarding the experimental values as a reference. Secondly, the motion equations used in our study are both based on classical mechanisms, thus all the quantum effects are not included. As a direct consequence, the statistical results would deviate from true values, especially in the low-temperature region. This issue could be addressed by introducing the quantum thermal bath (QTB) [66–68]. However, this technique is incompatible with our proposed scheme, where a key step involves performing an energy-conserving spin-lattice dynamics simulation to relax the system in a nonequilibrium state. On this occasion, the thermostats for both spin and lattice are switched off, and the motions are simulated within a classical framework. To ensure the self-consistency of our scheme, we believe it is more reasonable to use the classical heat bath in dynamics simulations.

### III. RESULTS

This section is divided into four parts. In Sec. III A, several test results are presented to validate the accuracy of SLD simulations, which are implemented in the PASP package. Subsequently, detailed calculations on three magnetic materials, namely  $\text{Y}_3\text{Fe}_5\text{O}_{12}$ ,  $\text{MnFe}_2\text{O}_4$ , and  $\text{Cr}_2\text{O}_3$ , are discussed in the rest parts.

#### A. Validations

In order to guarantee the reliability of our conclusions obtained from dynamics simulations, a series of pretests were carried out. We select some representative results and present them in Fig. 1, where  $\text{Cr}_2\text{O}_3$  is taken as the object to be studied.

Firstly, we set the ground state of  $\text{Cr}_2\text{O}_3$  as the initial state and performed a NVT simulation with  $T_{\text{set}} = 150\text{ K}$ . As shown in Fig. 1(a), the temperature of spin and lattice subsystems increased to 150 K in less than 5 ps and stayed there till the end. Since we can approximate  $E_k = 0.5E_L$  and  $E_p = 0.5E_L + E_S$ , Fig. 1(b) also indicates that the contribution of phonons and magnons to the excited state energy is around 87.5% and 12.5% respectively. This result could be verified from another perspective. Note that there are totally 10 atoms in the unit cell of  $\text{Cr}_2\text{O}_3$ , which contribute  $30k_B$  to the heat capacity. Meanwhile, the four magnetic atoms will contribute another  $4k_B$  in the low-temperature region. Therefore, we can estimate that the contribution of magnons to the total heat capacity is close to 11.8%, which is consistent with the result from dynamics simulations.

In Figs. 1(c) and 1(d), the initial state was set to be a nonequilibrium state with  $T_L = 30\text{ K}$  and  $T_S = 175\text{ K}$ . As we expected, the total energy was well conserved when the system evolved to equilibrium. In addition, the final temperature fell within the range 48–55 K, which agrees with our previous analysis of the heat capacities.

Lastly, we simulated the relaxation process using another nonequilibrium excited state with  $T_L = 180\text{ K}$  and  $T_S = 30\text{ K}$  as the initial state. As shown in Figs. 1(e) and 1(f), the temperature of spin system increased gradually to equilibrium with the total energy conserved throughout the simulation. Also, the final temperature is around 160 K, which matches well with our analysis. It should be pointed out that there exist two notable differences between this case and the previous. Firstly, the subsystems ultimately evolved to a same temperature in a finite time, which alleviated our concerns about the accuracy of SLD simulations. Besides, the relaxation time ( $\tau_2$ ) was

much longer than that ( $\tau_1$ ) in Fig. 1(c). For this phenomenon, a qualitative explanation is presented below.

Based on the theory of second quantization, the Hamiltonian model presented in Sec. II A can be expressed in the following form [69,70]:

$$H_L = \sum_{qp} \hbar\omega_{qp}(b_{qp}^\dagger b_{qp} + 1/2), \quad (19)$$

$$H_S = \sum_{\lambda} \epsilon_{\lambda} a_{\lambda}^\dagger a_{\lambda} + \text{Const.}, \quad (20)$$

$$W\{n_{\lambda-q}, n_{\lambda}, N_{qp} \rightarrow n_{\lambda-q} + 1, n_{\lambda} - 1, N_{qp} + 1\} = \frac{2\pi}{\hbar} |M_{\lambda,qp}|^2 (n_{\lambda-q} + 1)(n_{\lambda})(N_{qp} + 1) \delta(\epsilon_{\lambda-q} - \epsilon_{\lambda} + \hbar\omega_{qp}), \quad (22)$$

$$W\{n_{\lambda-q}, n_{\lambda}, N_{-qp} \rightarrow n_{\lambda-q} + 1, n_{\lambda} - 1, N_{-qp} - 1\} = \frac{2\pi}{\hbar} |M_{\lambda,qp}|^2 (n_{\lambda-q} + 1)(n_{\lambda})(N_{-qp}) \delta(\epsilon_{\lambda-q} - \epsilon_{\lambda} - \hbar\omega_{qp}), \quad (23)$$

where  $W$  represents the probability of one-phonon emission or absorption,  $n_{\lambda}$  denotes the occupation number of magnons, and  $N_{qp}$  stands for phonons. Both  $n_{\lambda}$  and  $N_{qp}$  can be estimated approximately using the Bose-Einstein distribution. According to the above formulas, the scattering rate  $W$  grows linearly with  $N$  and quadratically with  $n$ . Compared to Fig. 1(c), there are more phonons but fewer magnons in the case of Fig. 1(e), thus leading to a lower transition probability and a longer relaxation time. More technical details about the second quantization of interactions between phonons and magnons can be found in Ref. [69,70].

### B. Damping constants in $\text{Y}_3\text{Fe}_5\text{O}_{12}$

In the field of spintronics,  $\text{Y}_3\text{Fe}_5\text{O}_{12}$  (yttrium iron garnet, YIG) has gained much attention owing to its ultra-low magnetic damping [5–7]. The unique property of this material motivated us to investigate the intrinsic mechanism behind. Some previous studies have pointed out that spin-lattice interaction should be the main mechanism accounting for the magnetic damping in YIG, and they have also calculated the magnon-phonon relaxation time from a theoretical perspective [8]. However, their studies did not yield the numerical magnitude of damping directly, which is our target in this paper.

The crystal structure of YIG is presented in Fig. 2(a). There are totally 80 atoms in the primitive cell, of which 12 Fe ions are located in the center of oxygen tetrahedrons while the other eight Fe ions are sited in oxygen octahedrons. The magnetic ground state of YIG is illustrated in Fig. 2(b). Fe ions situated in different chemical environments contribute spins in opposite directions, which makes YIG a typical ferrimagnetic material.

In order to evaluate the Gilbert damping constants in YIG, our first step is to prepare an effective Hamiltonian model. Considering the balance between precision and efficiency, the cutoff radius of interactions was set to be 11.0 Bohr for atomic pairs and 6.7 Bohr for three-body clusters. After symmetry analyses, we identified 612 nonequivalent interactions in total, which included six Heisenberg exchange terms and nine spin-lattice coupling terms.

$$H_{SL} = \sum_{\lambda,qp} M_{\lambda,qp} a_{\lambda-q}^\dagger a_{\lambda} (b_{qp}^\dagger - b_{-qp}), \quad (21)$$

where  $b_{qp}$  denotes the annihilation operator of phonons with wave vector  $q$  in branch  $p$ , and  $a_{\lambda}$  represents the annihilation operator of magnons with wave vector  $\lambda$ . All the parameters, namely  $\omega_{qp}$ ,  $\epsilon_{\lambda}$ , and  $M_{\lambda,qp}$ , can be determined from the effective Hamiltonian model in principle. According to the Fermi's golden rule, we have

To determine the interaction parameters, we carried out a series of first-principles calculations, where a cubic cell was adopted to reduce the interference between adjacent cells caused by periodic boundary conditions. Following the settings in Ref. [49], we utilized the projector augmented-wave (PAW) method [71] and revised Perdew-Burke-Ernzerhof exchange-correlation functional for solids (PBEsol) [72] in our calculations. Besides, the DFT+U method in its simplified form [73] was employed where the effective Hubbard  $U$  parameter was set to be 4 eV for the  $3d$  electrons of Fe ions. In addition, a cutoff energy of 520 eV for plane wave basis

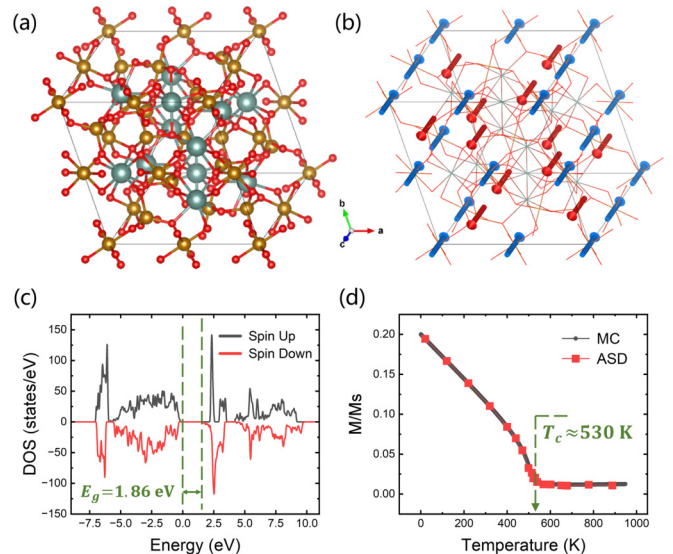


FIG. 2. (a) The primitive cell of  $\text{Y}_3\text{Fe}_5\text{O}_{12}$ . The golden balls represent iron atoms, the cyan balls stand for yttrium atoms, and the red balls represent oxygen atoms. (b) The magnetic ground state of YIG. The arrows of different colors represent the spin directions of Fe atoms. (c) The density of states obtained by DFT calculations. (d) The temperature dependence of average magnetization measured in MC and ASD simulations. For YIG, the phase transition point from ferrimagnetic to paramagnetic lies in 530 K approximately.

TABLE I. The Heisenberg exchange coefficients  $J$  (meV) of YIG, where an effective spin  $S = 1$  is used. For the  $\text{Fe}^O - \text{Fe}^O$  pairs, the Greek letters ( $\alpha$  and  $\beta$ ) refer to different chemical environments. The unit of distance is  $\text{\AA}$ .

Spin pair	Distance	$J$	Ref. [77]	Ref. [78]
$\text{Fe}^T - \text{Fe}^O$	3.445	47.414	39.63	42.50
$\text{Fe}^T - \text{Fe}^T$	3.774	2.399	2.81	3.25
$\text{Fe}^O - \text{Fe}^O (\alpha)$	5.337	0.538	0.50	0.00
$\text{Fe}^O - \text{Fe}^O (\beta)$	5.337	5.055		6.87
$\text{Fe}^T - \text{Fe}^O$	5.555	0.285	-0.50	-0.44
$\text{Fe}^T - \text{Fe}^T$	5.765	3.437	2.00	2.94

and a  $\Gamma$ -centered  $2 \times 2 \times 2$  mesh of  $k$  points were used in the DFT calculations.

In Fig. 2(c), we present the density of states (DOS) for YIG. With a band gap of 1.863 eV, there is hardly any electric current occurring in the low-temperature region. Moreover, the Heisenberg exchange coefficients of YIG are listed in Table I. To verify the accuracy of these parameters, we conducted both Monte Carlo (MC) and ASD simulations. The temperature dependence of average magnetization is shown in Fig. 2(d), which reveals the critical temperature of YIG to be 530 K. This result is slightly lower than the measured Curie temperature,  $T_C = 560$  K [5], but falls within our tolerance. Besides, we have used the linear spin wave theory [74,75] to obtain the magnon spectrum of YIG (see Fig. S1 within the Supplemental Material, SM [76]), which matches well with the published results [77]. The calculated values of coupling constants are provided in the SM [76].

Next, we come to deal with the force constant tensor. In order to demonstrate the impact of cutoff radius and validate the effectiveness of our optimization method, we present some results pertaining to the tensor of YIG in Table II. Here we use “VASP” to tag the original tensor obtained from DFT calculations, “PASP” to label the modified tensor in which interactions beyond the cutoff radius are eliminated, and “Modified” to label the tensor after optimization of independent variables. As shown in Table II, the “PASP” tensor violated the acoustic sum rule and was not positive semi-definite, whereas these issues were resolved for the

TABLE II. The force constant tensor of YIG. The columns labeled by A represent the sorted absolute values of  $\sum_j K_{ij,\alpha\beta}$  and the columns labeled by B list the sorted eigenvalues of  $K_{ij,\alpha\beta}$ . For the cubic cell of YIG, we obtained the original tensor with the VASP package. Then, we eliminated the elements that represent interactions beyond the cutoff radius. This step was done by PASP. Finally, the tensor was modified to meet the requirement of translational symmetry through the optimization formulated in Eq. (13).

No.	VASP		PASP		Modified	
	A	B	A	B	A	B
1	0.000	0.000	1.587	-0.102	0.000	0.000
2	0.000	0.000	1.587	-0.102	0.000	0.000
3	0.000	0.000	1.587	-0.102	0.000	0.000
4	0.000	1.065	1.587	0.643	0.000	0.444
5	0.000	1.065	1.587	0.643	0.000	0.444
6	0.000	1.065	1.587	0.643	0.000	0.444

“Modified” tensor. Although an obvious difference existed between the “PASP” and “Modified” tensor in terms of their eigenvalues, we still assumed the target system could be reasonably described by the “Modified” tensor and the validity of this assumption would be verified by the calculated results of damping constants. Additional details regarding the selection of tensor elements and the deviation of phonon spectra are provided in Fig. 3. According to Figs. 3(b) and 3(c), the major deviation in phonon spectra resulted from the elimination of tensor elements, rather than the subsequent modification.

Completing the preparation of Hamiltonian model, we applied the scheme proposed in Sec. II C to our first object,  $\text{Y}_3\text{Fe}_5\text{O}_{12}$ . An instance is presented in Fig. 4. We set  $T_L = 30$  K,  $T_S = 180$  K for the initial nonequilibrium state and used an expanded supercell, which contained 12 800 atoms in the simulation. Figure 4(a) shows the time evolution of spin temperature in different types of simulations. By comparing the curves, we could roughly estimate that the equivalent damping constant in SLD simulation fell within the range  $10^{-3}$ – $10^{-4}$ . To make the estimation more precise, we calculated the initial cooling rates  $\partial T_S / \partial t|_{t=0}$  through polynomial (or exponential) fittings and plotted them in Fig. 4(b). Afterwards, a linear regression was performed to determine the quantitative relation

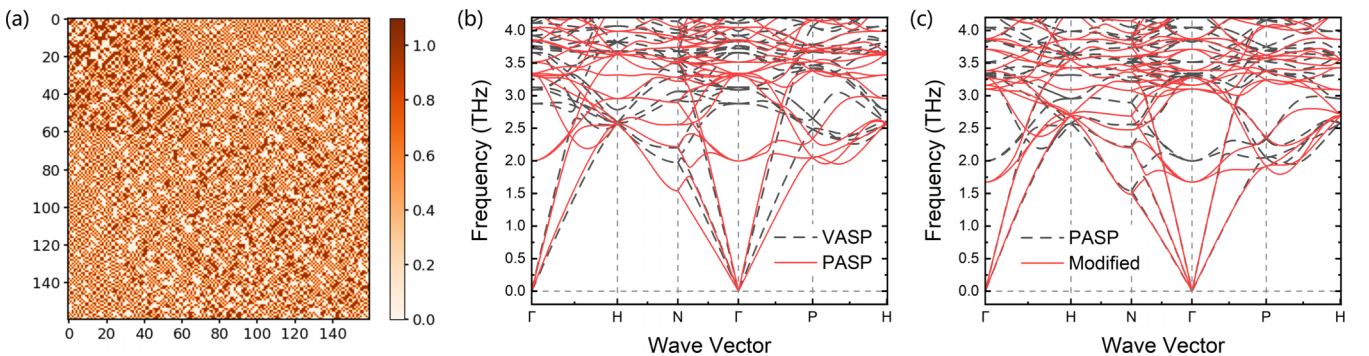


FIG. 3. (a) Visualization of selection on the force constant tensor elements for the cubic cell of YIG. A  $160 \times 160$  zero-one matrix is used to show the result of selection, in which “1” denotes the interactions within cutoff radius and “0” represents the elements that are artificially eliminated. (b) The phonon spectrum calculated from the force constant tensor before and after the elimination of tensor elements. (c) The phonon spectrum calculated from the force constant tensor before and after the optimization of independent variables.



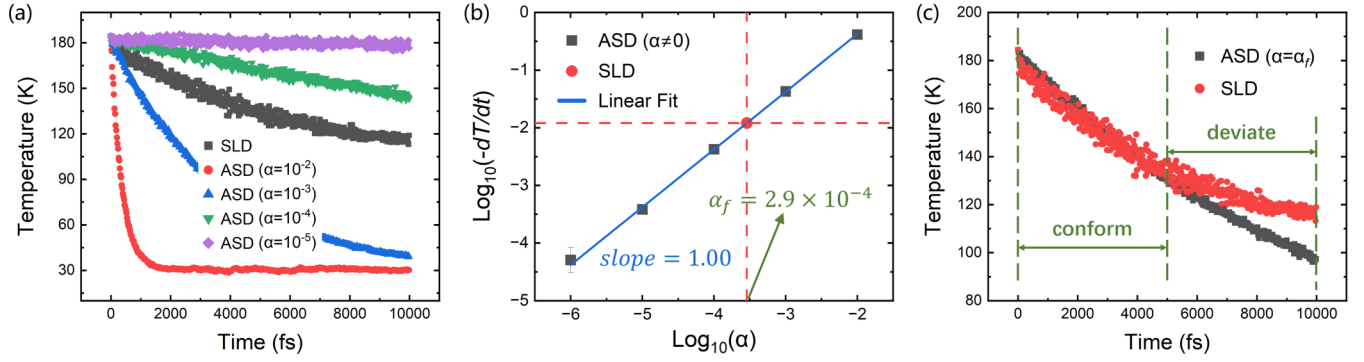


FIG. 4. (a) The time evolution of spin temperature in SLD and ASD simulations. The gray line represents the SLD simulation while the others refer to the ASD simulations with different damping constants. (b) The initial cooling rates  $\partial T_S/\partial t|_{t=0}$  with respect to the damping constants  $\alpha$ , where the scaling of axis is set to be logarithm. The gray squares refer to the results of ASD simulations and the blue line acts as the linear regression. The red circle is plotted by intersection of the blue line and the horizontal red dash line, which represents the initial cooling rate in the SLD simulation. Then we can obtain the equivalent damping constant from the abscissa of the red circle. (c) The comparison between ASD and SLD simulations. In the ASD simulation, the Gilbert damping constant is set to be  $\alpha = 2.9 \times 10^{-4}$ , which is exactly the result of our evaluation from the SLD simulation.

between  $\text{log}_{10}(-\partial T_S/\partial t|_{t=0})$  and  $\text{log}_{10}(\alpha)$ . As we expected, the cooling rates in ASD simulations were proportional to the assigned damping constants. Then, we combined the results of SLD and ASD simulations to evaluate the equivalent damping constant. This step was accomplished by identifying the intersection of red and blue lines in Fig. 4(b). Finally, the damping constant was determined to be  $\alpha_f = (2.9 \pm 0.5) \times 10^{-4}$  in this case. To verify our method and result, we present a comparison between SLD and ASD (where we set  $\alpha = \alpha_f$ ) simulations in Fig. 4(c). The curves agree well with each other in the initial stage but deviate in the second half. This phenomenon is within our expectation, because in the SLD simulation the lattice heats up as the spin cools down, thereby slowing the energy transfer between two subsystems.

In addition to the above instance, we have calculated the equivalent damping constants under different conditions to investigate the temperature dependence of magnetic damping. The final results are summarized in Fig. 5. Details about the estimation of uncertainties are given in the SM [76]. For  $\text{Y}_3\text{Fe}_5\text{O}_{12}$ , the damping constants at different temperatures stay on the order of  $10^{-4}$ , which are very close to the experimental values ( $3.2 \times 10^{-4}$  [79],  $2.2 \times 10^{-4}$  [80],  $1.2 - 1.7 \times 10^{-4}$  [81]). For example, the damping constant in bulk

YIG was reported as  $0.4 \times 10^{-4}$  in Ref. [82]. Meanwhile, our calculations yielded  $\alpha = (2.8 \pm 0.3) \times 10^{-5}$  at  $\Delta T = 15$  K and  $\alpha = (7.0 \pm 0.7) \times 10^{-5}$  at  $\Delta T = 30$  K, where both  $T_L = 0$  K. Thus, the result of experiments corresponds roughly to the temperature region of  $\Delta T = 15 \sim 30$  K in our study. Besides, Fig. 5 indicates that  $\alpha$  is approximately proportional to the temperature difference between two subsystems. This outcome is consistent with some computational studies in the past [33,35]. By comparing the subfigures in Fig. 5, we found little dependence of  $\alpha$  on the lattice temperature, although here  $T_L$  could be viewed as the ambient temperature of spin system.

As a supplement to Sec. III A, we further validate our simulations by analyzing the measured cooling rates in Fig. 5(a). By subtracting Eq. (23) from Eq. (22), the transfer rate of energy between magnon and phonon systems can be expressed as

$$\dot{Q} = \sum_{qp} \hbar \omega_{qp} \langle \dot{N}_{qp} \rangle = \sum_{\lambda, qp} T_{\lambda, qp}, \quad (24)$$

where  $T_{\lambda, qp}$  denotes different transfer channels,

$$T_{\lambda, qp} \propto (n_{\lambda} - n_{\lambda-q})N_{qp} + n_{\lambda-q}n_{\lambda} + n_{\lambda}. \quad (25)$$

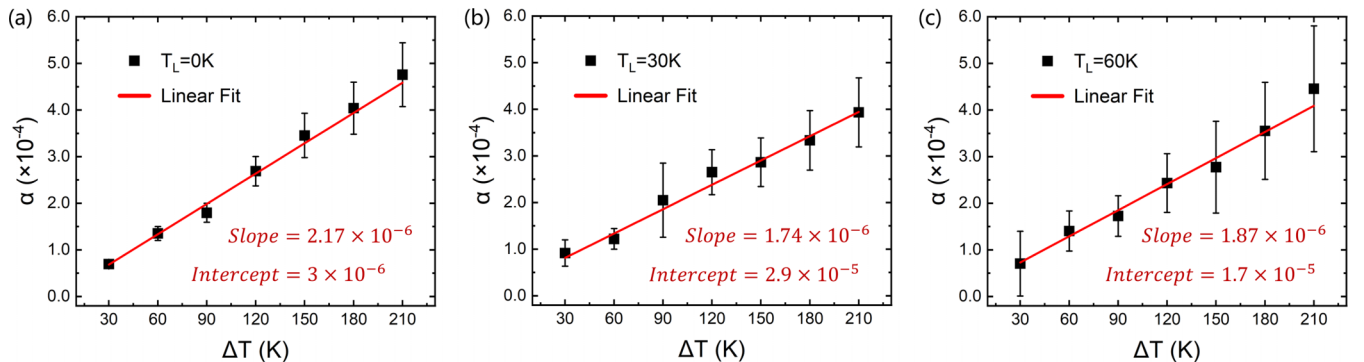


FIG. 5. The temperature dependence of Gilbert damping constants for  $\text{Y}_3\text{Fe}_5\text{O}_{12}$ . The label of abscissa axis  $\Delta T$  refers to  $T_S - T_L$  of the initial state in dynamical simulations. Measurements on the magnetic damping are performed under different initial conditions of the lattice temperature: (a)  $T_L = 0$  K, (b)  $T_L = 30$  K, (c)  $T_L = 60$  K.



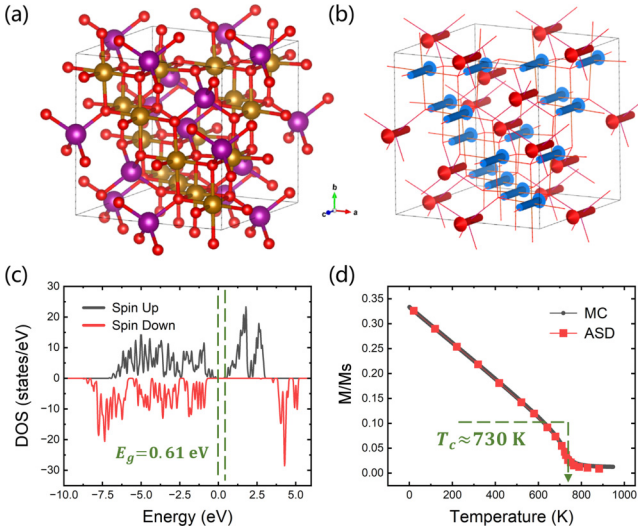


FIG. 6. (a) The cubic cell of  $\text{MnFe}_2\text{O}_4$ . The purple balls represent manganese atoms, the golden balls refer to iron atoms, and the red balls stand for oxygen atoms. (b) The magnetic ground state of MFO. The arrows of different colors represent the spin directions of Mn and Fe atoms separately. (c) The density of states obtained by DFT calculations. (d) The temperature dependence of average magnetization measured in MC and ASD simulations. For  $\text{MnFe}_2\text{O}_4$ , the phase transition point from ferrimagnetic to paramagnetic lies in 730 K approximately.

According to the Bose-Einstein distribution, the number of magnons and phonons can be expressed as

$$n_\lambda = \frac{1}{e^{\epsilon_\lambda/k_B T_S} - 1}, \quad N_{qp} = \frac{1}{e^{\hbar\omega_{qp}/k_B T_L} - 1}. \quad (26)$$

When  $T_S$  is high enough and  $T_L$  is close to zero, we can approximate  $n_\lambda = k_B T_S / \epsilon_\lambda \propto T_S$  and  $N_{qp}$  close to zero. Under these conditions, we have  $\dot{Q} \propto T_S^2$ . This relation was well verified by linear regressions and the results are provided in the supplementary material (see Fig. S4 within the SM [76]).

Furthermore, the accuracy of our simulations can also be proved from another perspective. According to Eqs. (22) and (23), the scattering rate  $W$  grows quadratically with the coupling parameters  $M_{\lambda,qp}$ . Based on the theory of second quantization,  $M_{\lambda,qp}$  shall be proportional to the coupling constants  $\partial J_{ij} / \partial u_{k,\alpha}$ . Thus under a definite condition of temperature, we have

$$\alpha \propto \dot{Q} \propto \Delta W \propto M_{\lambda,qp}^2 \propto (\partial J_{ij} / \partial u_{k,\alpha})^2. \quad (27)$$

To verify this relation, we adjusted the spin-lattice coupling constants of YIG while keeping the other model parameters unchanged. Subsequently, SLD simulations were carried out to evaluate the corresponding damping constants. The result is plotted in Fig. S5 within the SM [76], which agrees well with our predictions.

Since the spin-orbit coupling is typically believed to have an important contribution to the magnetic damping, we also calculated the exchange tensor of the nearest neighboring Fe-Fe pair in YIG using the four-state method, and repeated our scheme to evaluate the Gilbert damping constants. It turned out that taking the SOC effects into consideration only led to a small increase of around 5% in the estimated values. In

TABLE III. The exchange coefficients  $J$  in  $\text{MnFe}_2\text{O}_4$ , where an effective spin  $S = 1$  is adopted. The unit of distance is  $\text{\AA}$ . We note that the exchange coefficients listed here were calculated by different Hubbard parameters (eV):  $U_{\text{Mn}} = 3.3$  and  $U_{\text{Fe}} = 3.6$  in this paper;  $U_{\text{Mn}} = 4.0$ ,  $J_{\text{Mn}} = 0.7$ ,  $U_{\text{Fe}} = 4.5$ ,  $J_{\text{Fe}} = 0.89$  in Ref. [84].

Spin pair	Distance	$J$ (meV)	Ref. [84]
1NN Fe-Fe	3.003	6.835	4.5
1NN Mn-Fe	3.521	33.224	22.5
1NN Mn-Mn	3.667	3.956	
2NN Fe-Fe	5.201	0.929	0.0

addition, we have followed the steps in Ref. [35] to calculate the damping parameters in YIG. The results confirmed that without SOC effects the uniform magnon mode ( $q=0$ ) would not be damped [24]. The above calculations are detailed in the supplementary material.

### C. Damping constants in $\text{MnFe}_2\text{O}_4$

After the calculation on YIG, we applied our method to  $\text{MnFe}_2\text{O}_4$  (MFO), which was reported to possess a large Gilbert damping constant in the literature [20,83]. As shown in Fig. 6(a),  $\text{MnFe}_2\text{O}_4$  has a typical structure of spinels, where A sites are surrounded by four oxygen atoms and B sites are located in octahedrons. Generally, spinels can be classified into normal and inverse structures according to the distribution of divalent and trivalent cations between A/B sites. In experiments, MFO usually crystallizes into a mixed phase where the normal structure occupies the major part (80% in bulk MFO [84]). Here, we only considered its normal structure in this paper. Also, the magnetic ground state of MFO is shown in Fig. 6(b), where the magnetic moments are antiparallel between A/B sites.

Firstly, we started to construct an effective Hamiltonian model for MFO. With the same cutoff settings for YIG, we found 105 nonequivalent interactions, including four Heisenberg exchange terms and 10 spin-lattice coupling terms. Subsequently, DFT calculations were carried out to determine the interaction parameters. In these calculations, we adopted a cubic cell containing 56 atoms and a  $\Gamma$ -centered  $4 \times 4 \times 4$  grid mesh in the reciprocal space. Besides,  $U_{\text{Mn}} = 3.3$  eV and  $U_{\text{Fe}} = 3.6$  eV were used as the effective Hubbard parameters [84]. With the exception of aforementioned settings, all the relevant first-principles calculations were performed under the same conditions as in Sec. III B.

The DOS of  $\text{MnFe}_2\text{O}_4$  is plotted in Fig. 6(c), yielding a calculated band gap of 0.612 eV. This value does not match with the result of transport experiments, which reported a much smaller band gap (0.04–0.06 eV) [25]. In addition, MC and ASD simulations were performed using the Heisenberg exchange coefficients listed in Table III. The temperature dependence of average magnetization, shown in Fig. 6(d), suggests the critical temperature to be around 730 K. This result is significantly higher than the measured value of 573 K [85]. Both of the above discrepancies may be attributed to the inevitable difference between the ideal normal spinel structure in calculations and the partially disordered samples in reality. Despite this problem, we proceeded to describe the

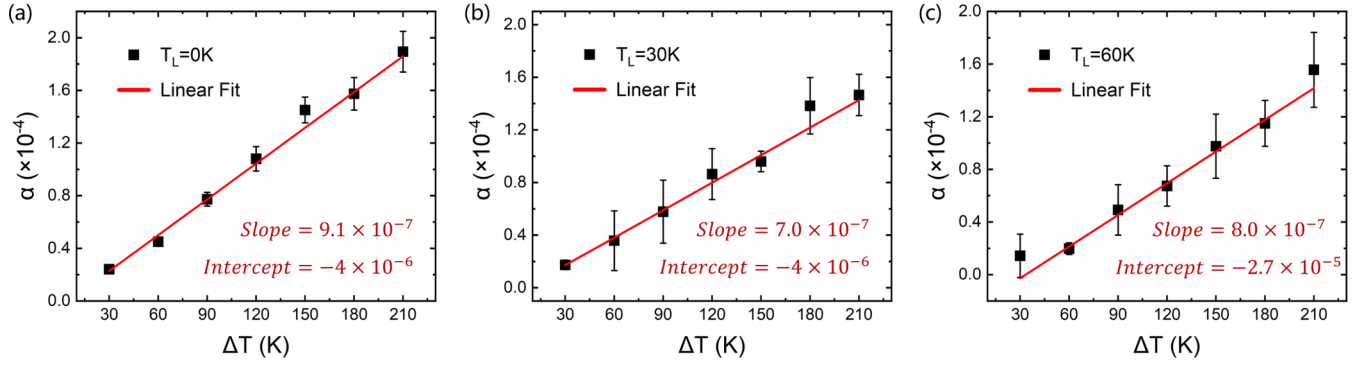


FIG. 7. The temperature dependence of Gilbert damping constants for  $\text{MnFe}_2\text{O}_4$ . The label of abscissa axis  $\Delta T$  refers to  $T_S - T_L$  of the initial state in dynamical simulations. Measurements on the magnetic damping are performed under different initial conditions of the lattice temperature: (a)  $T_L = 0$  K, (b)  $T_L = 30$  K, (c)  $T_L = 60$  K.

target system with our Hamiltonian model and expected to see how far the calculated results of damping constants would differ from experimental values.

After the preparation of Hamiltonian model, we conducted dynamics simulations to evaluate the equivalent damping parameters in MFO at different temperatures. A supercell containing 13 440 atoms was adopted in the simulation, and the results are summarized in Fig. 7. The average of calculated damping constants is around  $8 \times 10^{-5}$ , which is much smaller than the measured value,  $1.0 \times 10^{-2}$  [20,83]. Two factors may account for this inconsistency. Firstly, the inhomogeneity in real  $\text{MnFe}_2\text{O}_4$  samples greatly enhances the scattering of magnons and phonons, thereby increasing the damping constants. Additionally, due to the narrow band gap observed in experiments, eddy currents can arise at finite temperatures, which leads to a rapid loss of energy in the form of joule heat. As the result of these factors, we failed to obtain a reason-

able estimation of Gilbert damping constants for  $\text{MnFe}_2\text{O}_4$  with our methodology. On the other side, the contribution of different relaxation mechanisms to FMR linewidth has been studied comprehensively for  $\text{MnFe}_2\text{O}_4$  in Ref. [25], which further confirms our analyses.

#### D. Damping constants in $\text{Cr}_2\text{O}_3$

Chromia ( $\text{Cr}_2\text{O}_3$ ) is a well-known collinear magnetoelectric antiferromagnet, which holds great prospects in the field of spintronics [86–88]. As shown in Fig. 8(a), the primitive cell of  $\text{Cr}_2\text{O}_3$  contains 10 atoms, with each chromium atom bonded to the six oxygen atoms around it. Additionally, Fig. 8(b) displays the magnetic ground state of  $\text{Cr}_2\text{O}_3$ , where the spins of two nearest-neighbor Cr atoms are oriented in opposite directions.

As a preliminary step in constructing the Hamiltonian model, we set the cutoff radius of interactions to be 11.0 Bohr for atomic pairs and 7.0 Bohr for three-body clusters. Through symmetry analyses, we identified 319 nonequivalent interactions, including five Heisenberg exchange terms and 21 spin-lattice coupling terms.

Afterwards, a series of first-principles calculations were performed to determine the model parameters. Following the settings in Ref. [89], we adopted a hexagonal cell of  $\text{Cr}_2\text{O}_3$ , which contained a total of 90 atoms in the calculations. Additionally, we used the LSDA+U method in its full spherically symmetric form [90]. As to the Hubbard parameters,  $J$  was fixed at its recommended value of 0.6 eV, and  $U$  was adjusted to fit the Néel temperature observed in experiments [91]. We found  $U = 2.0$  eV was the optimal value for  $3d$  electrons of Cr ions. Except for the settings specified above, all the DFT calculations were conducted under the same conditions as in Sec. III C.

The DOS of  $\text{Cr}_2\text{O}_3$  is plotted in Fig. 8(c), which yields a band gap of 1.935 eV. This value indicates that the energy dissipation of electric currents can be neglected in this system. Additionally, we list the calculated exchange coefficients of chromia and some published results in Table IV. Both MC and ASD simulations were performed to investigate the temperature dependence of sublattice magnetization. According to Fig. 8(d), the critical point was determined to be 310 K approximately, which was quite consistent with the experimental

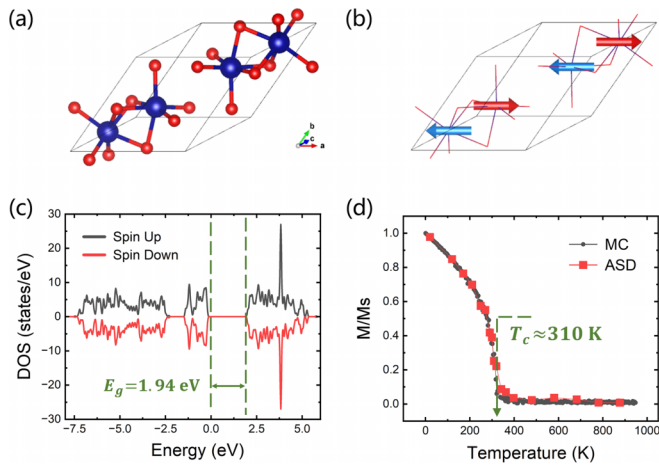


FIG. 8. (a) The primitive cell of  $\text{Cr}_2\text{O}_3$ . The dark-blue balls represent chromium atoms, and the red balls stand for oxygen atoms. (b) The magnetic ground state. The arrows of different colors represent the spin directions of Cr atoms. (c) The density of states obtained by DFT calculations. (d) The temperature dependence of sublattice magnetization measured in MC and ASD simulations. For  $\text{Cr}_2\text{O}_3$ , the phase transition point from ferrimagnetic to paramagnetic lies in 310 K approximately.

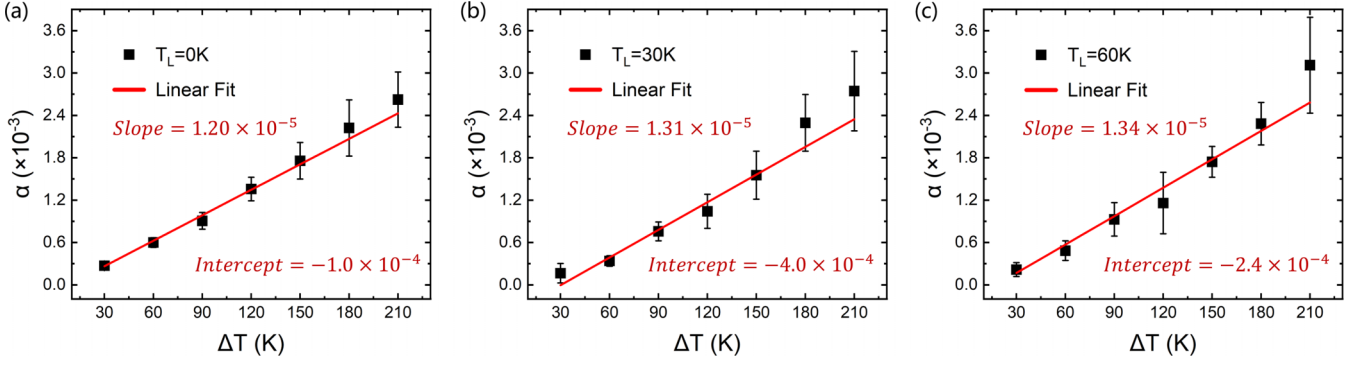


FIG. 9. The temperature dependence of Gilbert damping constants for  $\text{Cr}_2\text{O}_3$ . The label of abscissa axis  $\Delta T$  refers to  $T_S - T_L$  of the initial state in dynamical simulations. Measurements on the magnetic damping are performed under different initial conditions of the lattice temperature: (a)  $T_L = 0$  K, (b)  $T_L = 30$  K, (c)  $T_L = 60$  K.

value. Similarly, the force constants of  $\text{Cr}_2\text{O}_3$  went through the modification formulated in Sec. II B, and the spin-lattice coupling parameters are provided in the SM [76].

After the construction of Hamiltonian model, we conducted a series of dynamics simulations to evaluate the equivalent damping parameters in  $\text{Cr}_2\text{O}_3$ . An expanded hexagonal cell containing 14 400 atoms was adopted for the simulation, and the results are summarized in Fig. 9. As two specific cases, our calculation yielded  $\alpha = (1.31 \pm 0.14) \times 10^{-4}$  at  $\Delta T = 15$  K and  $\alpha = (2.7 \pm 0.3) \times 10^{-4}$  at  $\Delta T = 30$  K, where both  $T_L = 0$  K. Therefore, the calculated damping constants within  $\Delta T = 15 \sim 30$  K are quite close to  $2 \times 10^{-4}$ , which is the estimated value reported in Ref. [92].

Furthermore, the damping constants in  $\text{Cr}_2\text{O}_3$  exhibit a significant nonlinear relation with the temperature difference of subsystems. Through logarithmic fittings, we calculated the power exponents for Figs. 9(a)–9(c), and the results were 1.17, 1.62, 1.38. If we disregard the difference between  $\Delta T$  and  $T$  for the moment, these values are in good agreement with the theoretical prediction of Kasuya and LeCraw [38]. According to their study, the relaxation rate varies as  $T^n$  where  $n = 1 \sim 2$  while  $n = 2$  corresponds to a larger regime of temperature.

Compared to YIG, the greater magnetic damping calculated for chromia can be attributed to its significantly stronger spin-lattice coupling. As shown in Fig. 10, the magnitude of principal spin-lattice coupling constant in  $\text{Cr}_2\text{O}_3$  is two or

three times larger than that in YIG. This could be explained by the fact that direct exchange interaction between two magnetic atoms decreases rapidly with their distance but the change becomes slower gradually [93]. Therefore, owing to the shorter distance of Cr-Cr pair, the direct exchange interaction between neighboring Cr atoms could have a major contribution to the stronger spin-lattice coupling in  $\text{Cr}_2\text{O}_3$ .

#### IV. CONCLUSIONS

In summary, we put forward a scheme to estimate the Gilbert damping parameters contributed by spin-lattice coupling in insulating magnetic materials. The methodology involves first-principles-based Hamiltonian models and spin-lattice dynamics simulations. Although our results do not correspond directly to the measurements of FMR experiments, the calculated damping constant can be a suitable input for micromagnetic simulations. Following a series of validations, we applied our method to  $\text{Y}_3\text{Fe}_5\text{O}_{12}$ ,  $\text{MnFe}_2\text{O}_4$ , and  $\text{Cr}_2\text{O}_3$ . Under specific temperature conditions, the results for YIG and  $\text{Cr}_2\text{O}_3$  were close to the experimental values, while the large discrepancy in MFO could be attributed to the inhomogeneity and small band gap in real samples. In addition, we confirmed a quasilinear dependence of damping constants on the temperature difference between spin and lattice subsystems. Overall, the approach presented in this paper holds promise for effectively evaluating the damping in magnetic insulators.

TABLE IV. The Heisenberg exchange coefficients  $J$  (meV) of  $\text{Cr}_2\text{O}_3$ , where an effective spin  $S = 1$  is adopted. The unit of distance is  $\text{\AA}$ . We note that the exchange coefficients listed here were calculated by different Hubbard parameters (eV):  $U = 2.0$  and  $J = 0.6$  in this paper,  $U = 4.0$  and  $J = 0.5$  in Ref. [51],  $U = 2.5$  and  $J = 0.58$  in Ref. [89].

Spin pair.	Distance	$J$	Ref. [51]	Ref. [89]
1NN Cr-Cr	2.640	44.778	25.4	30.9
2NN Cr-Cr	2.873	29.269	21.2	21.9
3NN Cr-Cr	3.411	-0.182	-3.9	-0.60
4NN Cr-Cr	3.635	0.007	-3.3	-1.83
5NN Cr-Cr	4.137	-0.500	4.2	4.92

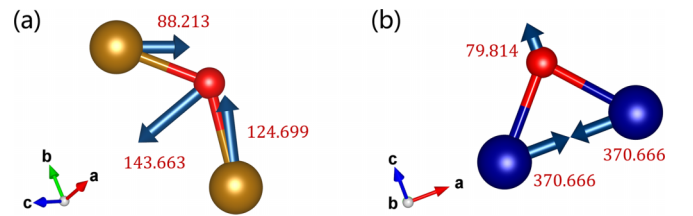


FIG. 10. (a) The 1NN  $\text{Fe}^T\text{-Fe}^O$  pair in  $\text{Y}_3\text{Fe}_5\text{O}_{12}$ . (b) The 1NN Cr-Cr pair in  $\text{Cr}_2\text{O}_3$ . The steel-blue arrow stands for the orientation of  $\partial J/\partial u$  and the red number along with it represents the magnitude in unit of  $\text{meV}/\text{\AA}$ .

## ACKNOWLEDGMENTS

This work is supported by the National Key R&D Program of China (No. 2022YFA1402901), the National Natural Science Foundation of China (Grants No. 11825403, No. 11991061, and No. 12188101), the Guangdong Major Project of the Basic and Applied Basic Research (Future functional materials under extreme conditions–2021B0301030005).

## APPENDIX: COOLING RATES AND DAMPING

Here, we would like to derive the relation between cooling rates  $\partial T_S/\partial t$  and damping constants  $\alpha$ ,

$$\begin{aligned} \frac{\partial T_S}{\partial t} &= \frac{1}{C_{\text{spin}}} \frac{\partial E_{\text{mag}}}{\partial t} = \frac{1}{C_{\text{spin}}} \frac{\partial}{\partial t} \left( -\frac{1}{2} \sum_i \mathbf{m}_i \cdot \mathbf{B}_i^{\text{eff}} \right) \\ &\propto - \sum_i \frac{\partial \mathbf{m}_i}{\partial t} \cdot \mathbf{B}_i^{\text{eff}} - \sum_i \mathbf{m}_i \cdot \frac{\partial \mathbf{B}_i^{\text{eff}}}{\partial t}, \end{aligned} \quad (\text{A1})$$

where  $C_{\text{spin}}$  and  $E_{\text{mag}}$  denote the specific heat and total energy of spin subsystem respectively. Then,

we have

$$\begin{aligned} \frac{\partial \mathbf{m}_i}{\partial t} \cdot \mathbf{B}_i^{\text{eff}} &= \left( -\gamma \mathbf{m}_i \times \mathbf{B}_i^{\text{eff}} + \frac{\alpha}{|\mathbf{m}_i|} \mathbf{m}_i \times \frac{\partial \mathbf{m}_i}{\partial t} \right) \cdot \mathbf{B}_i^{\text{eff}} \\ &= \left( \frac{\alpha}{|\mathbf{m}_i|} \mathbf{m}_i \times \frac{\partial \mathbf{m}_i}{\partial t} \right) \cdot \mathbf{B}_i^{\text{eff}} \propto \alpha, \end{aligned} \quad (\text{A2})$$

$$\begin{aligned} \mathbf{m}_i \cdot \frac{\partial \mathbf{B}_i^{\text{eff}}}{\partial t} &= \mathbf{m}_i \cdot \left( \sum_j \frac{\partial \mathbf{B}_i^{\text{eff}}}{\partial \mathbf{m}_j} \frac{\partial \mathbf{m}_j}{\partial t} \right) = \sum_{(i,j)} C_{ij} \mathbf{m}_i \cdot \frac{\partial \mathbf{m}_j}{\partial t} \\ &= \sum_{(i,j)} C_{ij} \mathbf{m}_i \cdot \left( -\gamma \mathbf{m}_j \times \mathbf{B}_j^{\text{eff}} + \frac{\alpha}{|\mathbf{m}_j|} \mathbf{m}_j \times \frac{\partial \mathbf{m}_j}{\partial t} \right) \\ &= \alpha \sum_{(i,j)} (\dots) - \sum_{(i,j)} \sum_{(j,k)} C_{ij} C_{jk} \gamma \mathbf{m}_i \cdot (\mathbf{m}_j \times \mathbf{m}_k) \\ &= \alpha \sum_{(i,j)} C_{ij} \mathbf{m}_i \cdot \left( \frac{\mathbf{m}_j}{|\mathbf{m}_j|} \times \frac{\partial \mathbf{m}_j}{\partial t} \right), \end{aligned} \quad (\text{A3})$$

in which we express the effective magnetic field as  $\mathbf{B}_i^{\text{eff}} = \sum_{(i,j)} C_{ij} \mathbf{m}_j$ . Here the symbol  $\sum_{(i,j)}$  means summing the index  $j$ , which satisfies that  $j$ th site is one of the nearest neighbors to  $i$ th site. As demonstrated below, the second term in the third line of Eq. (A3) does not contribute to the result,

$$\begin{aligned} \sum_i \sum_{(i,j)} \sum_{(j,k)} C_{ij} C_{jk} \mathbf{m}_i \cdot (\mathbf{m}_j \times \mathbf{m}_k) &= \frac{1}{2} \sum_i \sum_{(i,j)} \sum_{(j,k)} [C_{ij} C_{jk} \mathbf{m}_i \cdot (\mathbf{m}_j \times \mathbf{m}_k) + C_{kj} C_{ji} \mathbf{m}_k \cdot (\mathbf{m}_j \times \mathbf{m}_i)] \\ &= \frac{1}{2} \sum_i \sum_{(i,j)} \sum_{(j,k)} [C_{ij} C_{jk} \mathbf{m}_i \cdot (\mathbf{m}_j \times \mathbf{m}_k) + C_{jk} C_{ij} \mathbf{m}_i \cdot (\mathbf{m}_k \times \mathbf{m}_j)] = 0. \end{aligned} \quad (\text{A4})$$

Combining the above equations, we come to the conclusion that  $\partial T_S/\partial t$  is proportional to  $\alpha$ . This relation is derived at the lowest order of approximation, where we neglect the

higher orders of  $\alpha$  and only consider the isotropic exchange interaction in the model. We believe these approximations are reasonable for the compounds studied in this paper.

- [1] S. Wolf, D. Awschalom, R. Buhrman, J. Daughton, S. von Molnar, M. Roukes, A. Chtchelkanova, and D. Treger, Spintronics: A spin-based electronics vision for the future, *Science* **294**, 1488 (2001).
- [2] T. Jungwirth, X. Marti, P. Wadley, and J. Wunderlich, Antiferromagnetic spintronics, *Nat. Nanotechnol.* **11**, 231 (2016).
- [3] L. Šmejkal, Y. Mokrousov, B. Yan, and A. H. MacDonald, Topological antiferromagnetic spintronics, *Nat. Phys.* **14**, 242 (2018).
- [4] I. Žutić, J. Fabian, and S. Das Sarma, Spintronics: Fundamentals and applications, *Rev. Mod. Phys.* **76**, 323 (2004).
- [5] V. Cherepanov, I. Kolokolov, and V. L'vov, The saga of YIG: Spectra, thermodynamics, interaction and relaxation of magnons in a complex magnet, *Phys. Rep.* **229**, 81 (1993).
- [6] A. A. Serga, A. V. Chumak, and B. Hillebrands, YIG magnonics, *J. Phys. D: Appl. Phys.* **43**, 264002 (2010).
- [7] H. Wang, C. Du, P. C. Hammel, and F. Yang, Spin transport in antiferromagnetic insulators mediated by magnetic correlations, *Phys. Rev. B* **91**, 220410(R) (2015).

- [8] Y. Liu, L.-S. Xie, Z. Yuan, and K. Xia, Magnon-phonon relaxation in yttrium iron garnet from first principles, *Phys. Rev. B* **96**, 174416 (2017).
- [9] T. Gilbert, A phenomenological theory of damping in ferromagnetic materials, *IEEE Trans. Magn.* **40**, 3443 (2004).
- [10] D. Thonig, Y. Kvashnin, O. Eriksson, and M. Pereiro, Nonlocal Gilbert damping tensor within the torque-torque correlation model, *Phys. Rev. Mater.* **2**, 013801 (2018).
- [11] A. Brataas, Y. Tserkovnyak, and G. E. W. Bauer, Scattering theory of Gilbert damping, *Phys. Rev. Lett.* **101**, 037207 (2008).
- [12] M. Fähnle, D. Steiauf, and J. Seib, The Gilbert equation revisited: Anisotropic and nonlocal damping of magnetization dynamics, *J. Phys. D: Appl. Phys.* **41**, 164014 (2008).
- [13] K. Gilmore and M. D. Stiles, Evaluating the locality of intrinsic precession damping in transition metals, *Phys. Rev. B* **79**, 132407 (2009).
- [14] K. Gilmore, M. D. Stiles, J. Seib, D. Steiauf, and M. Fähnle, Anisotropic damping of the magnetization dynamics in Ni, Co, and Fe, *Phys. Rev. B* **81**, 174414 (2010).



- [15] A. Vansteenkiste, J. Leliaert, M. Dvornik, M. Helsen, F. Garcia-Sanchez, and B. Van Waeyenberge, The design and verification of MuMax3, *AIP Adv.* **4**, 107133 (2014).
- [16] I. P. Miranda, A. B. Klautau, A. Bergman, D. Thonig, H. M. Petrilli, and O. Eriksson, Mechanisms behind large Gilbert damping anisotropies, *Phys. Rev. B* **103**, L220405 (2021).
- [17] S. Karakurt, R. Chantrell, and U. Nowak, A model of damping due to spin–lattice interaction, *J. Magn. Magn. Mater.* **316**, e280 (2007).
- [18] M. C. Hickey and J. S. Moodera, Origin of intrinsic Gilbert damping, *Phys. Rev. Lett.* **102**, 137601 (2009).
- [19] A. Widom, C. Vittoria, and S. Yoon, Gilbert ferromagnetic damping theory and the fluctuation-dissipation theorem, *J. Appl. Phys.* **108**, 073924 (2010).
- [20] C. Vittoria, S. D. Yoon, and A. Widom, Relaxation mechanism for ordered magnetic materials, *Phys. Rev. B* **81**, 014412 (2010).
- [21] O. Eriksson, A. Bergman, L. Bergqvist, and J. Hellsvik, *Atomistic Spin Dynamics: Foundations and Applications* (Oxford University Press, Oxford, 2017).
- [22] R. F. L. Evans, W. J. Fan, P. Chureemart, T. A. Ostler, M. O. A. Ellis, and R. W. Chantrell, Atomistic spin model simulations of magnetic nanomaterials, *J. Phys.: Condens. Matter* **26**, 103202 (2014).
- [23] H. Suhl, *Relaxation Processes in Micromagnetics*, International Series of Monographs on Physics Vol. 133 (Oxford University Press, Oxford, 2007).
- [24] S. Azzawi, A. T. Hindmarch, and D. Atkinson, Magnetic damping phenomena in ferromagnetic thin-films and multilayers, *J. Phys. D* **50**, 473001 (2017).
- [25] A. G. Flores, V. Raposo, L. Torres, and J. Iñiguez, Two-magnon processes and ferrimagnetic linewidth calculation in manganese ferrite, *Phys. Rev. B* **59**, 9447 (1999).
- [26] K. Zakeri, J. Lindner, I. Barsukov, R. Meckenstock, M. Farle, U. von Hörsten, H. Wende, W. Keune, J. Rucker, S. S. Kalarickal, K. Lenz, W. Kuch, K. Baberschke, and Z. Frait, Spin dynamics in ferromagnets: Gilbert damping and two-magnon scattering, *Phys. Rev. B* **76**, 104416 (2007).
- [27] V. Kamberský, On ferromagnetic resonance damping in metals, *Czech. J. Phys.* **B 26**, 1366 (1976).
- [28] D. Steiauf and M. Fähnle, Damping of spin dynamics in nanostructures: An *ab initio* study, *Phys. Rev. B* **72**, 064450 (2005).
- [29] K. Gilmore, Y. U. Idzerda, and M. D. Stiles, Identification of the dominant precession-damping mechanism in Fe, Co, and Ni by first-principles calculations, *Phys. Rev. Lett.* **99**, 027204 (2007).
- [30] V. Kamberský, Spin-orbital Gilbert damping in common magnetic metals, *Phys. Rev. B* **76**, 134416 (2007).
- [31] H. Ebert, S. Mankovsky, D. Ködderitzsch, and P. J. Kelly, *Ab initio* calculation of the Gilbert damping parameter via the linear response formalism, *Phys. Rev. Lett.* **107**, 066603 (2011).
- [32] S. Mankovsky, D. Ködderitzsch, G. Woltersdorf, and H. Ebert, First-principles calculation of the Gilbert damping parameter via the linear response formalism with application to magnetic transition metals and alloys, *Phys. Rev. B* **87**, 014430 (2013).
- [33] M. Abmann and U. Nowak, Spin-lattice relaxation beyond Gilbert damping, *J. Magn. Magn. Mater.* **469**, 217 (2019).
- [34] J. Tranchida, S. Plimpton, P. Thibaudeau, and A. Thompson, Massively parallel symplectic algorithm for coupled magnetic spin dynamics and molecular dynamics, *J. Comput. Phys.* **372**, 406 (2018).
- [35] M. Strungaru, M. O. A. Ellis, S. Ruta, O. Chubykalo-Fesenko, R. F. L. Evans, and R. W. Chantrell, Spin-lattice dynamics model with angular momentum transfer for canonical and microcanonical ensembles, *Phys. Rev. B* **103**, 024429 (2021).
- [36] S. Pavaskar, R. Penco, and I. Z. Rothstein, An effective field theory of magneto-elasticity, *SciPost Phys.* **12**, 155 (2022).
- [37] S. Streib, N. Vidal-Silva, K. Shen, and G. E. W. Bauer, Magnon-phonon interactions in magnetic insulators, *Phys. Rev. B* **99**, 184442 (2019).
- [38] T. Kasuya and R. C. LeCraw, Relaxation mechanisms in ferromagnetic resonance, *Phys. Rev. Lett.* **6**, 223 (1961).
- [39] A. Rückriegel, S. Streib, G. E. W. Bauer, and R. A. Duine, Angular momentum conservation and phonon spin in magnetic insulators, *Phys. Rev. B* **101**, 104402 (2020).
- [40] S. Mankovsky, S. Polesya, H. Lange, M. Weißenhofer, U. Nowak, and H. Ebert, Angular momentum transfer via relativistic spin-lattice coupling from first principles, *Phys. Rev. Lett.* **129**, 067202 (2022).
- [41] F. Lou, X. Li, J. Ji, H. Yu, J. Feng, X. Gong, and H. Xiang, PAsP: Property analysis and simulation package for materials, *J. Chem. Phys.* **154**, 114103 (2021).
- [42] H. J. Xiang, E. J. Kan, S.-H. Wei, M.-H. Whangbo, and X. G. Gong, Predicting the spin-lattice order of frustrated systems from first principles, *Phys. Rev. B* **84**, 224429 (2011).
- [43] H. Xiang, C. Lee, H.-J. Koo, X. Gong, and M.-H. Whangbo, Magnetic properties and energy-mapping analysis, *Dalton Trans.* **42**, 823 (2013).
- [44] X. Z. Lu, M.-H. Whangbo, S. Dong, X. G. Gong, and H. J. Xiang, Giant ferroelectric polarization of  $\text{CaMn}_7\text{O}_{12}$  induced by a combined effect of Dzyaloshinskii-Moriya interaction and exchange striction, *Phys. Rev. Lett.* **108**, 187204 (2012).
- [45] C. Gong, L. Li, Z. Li, H. Ji, A. Stern, Y. Xia, T. Cao, W. Bao, C. Wang, Y. Wang *et al.*, Discovery of intrinsic ferromagnetism in two-dimensional van der Waals crystals, *Nature (London)* **546**, 265 (2017).
- [46] C. Xu, J. Feng, H. Xiang, and L. Bellaiche, Interplay between Kitaev interaction and single ion anisotropy in ferromagnetic  $\text{CrI}_3$  and  $\text{CrGeTe}_3$  monolayers, *npj Comput. Mater.* **4**, 57 (2018).
- [47] Y. Deng, Y. Yu, Y. Song, J. Zhang, N. Z. Wang, Z. Sun, Y. Yi, Y. Z. Wu, S. Wu, J. Zhu *et al.*, Gate-tunable room-temperature ferromagnetism in two-dimensional  $\text{Fe}_3\text{GeTe}_2$ , *Nature (London)* **563**, 94 (2018).
- [48] C. Xu, B. Xu, B. Dupé, and L. Bellaiche, Magnetic interactions in  $\text{BiFeO}_3$ : A first-principles study, *Phys. Rev. B* **99**, 104420 (2019).
- [49] D. Campbell, C. Xu, T. Bayarar, and L. Bellaiche, Finite-temperature properties of rare-earth iron garnets in a magnetic field, *Phys. Rev. B* **102**, 144406 (2020).
- [50] J. Y. Ni, X. Y. Li, D. Amoroso, X. He, J. S. Feng, E. J. Kan, S. Picozzi, and H. J. Xiang, Giant biquadratic exchange in 2D magnets and its role in stabilizing ferromagnetism of  $\text{NiCl}_2$  monolayers, *Phys. Rev. Lett.* **127**, 247204 (2021).
- [51] M. Fechner, A. Sukhov, L. Chotorlishvili, C. Kenel, J. Berakdar, and N. A. Spaldin, Magnetophononics: Ultrafast spin control through the lattice, *Phys. Rev. Mater.* **2**, 064401 (2018).

- [52] X. He, N. Helbig, M. J. Verstraete, and E. Bousquet, TB2J: A python package for computing magnetic interaction parameters, *Comput. Phys. Commun.* **264**, 107938 (2021).
- [53] H. Zhu, P. Liu, X. Zuo, and B. Shao, Magnetic ground state of CrOCl: A first-principles study, *Phys. Rev. B* **108**, 094435 (2023).
- [54] A. Togo and I. Tanaka, First principles phonon calculations in materials science, *Scr. Mater.* **108**, 1 (2015).
- [55] X. Gonze, J.-C. Charlier, D. C. Allan, and M. P. Teter, Interatomic force constants from first principles: The case of  $\alpha$ -quartz, *Phys. Rev. B* **50**, 13035 (1994).
- [56] X. Gonze and C. Lee, Dynamical matrices, born effective charges, dielectric permittivity tensors, and interatomic force constants from density-functional perturbation theory, *Phys. Rev. B* **55**, 10355 (1997).
- [57] G. Kresse and J. Hafner, *Ab initio* molecular dynamics for open-shell transition metals, *Phys. Rev. B* **48**, 13115 (1993).
- [58] G. Kresse and J. Furthmüller, Efficient iterative schemes for *ab initio* total-energy calculations using a plane-wave basis set, *Phys. Rev. B* **54**, 11169 (1996).
- [59] G. Kresse and J. Furthmüller, Efficiency of *ab-initio* total energy calculations for metals and semiconductors using a plane-wave basis set, *Comput. Mater. Sci.* **6**, 15 (1996).
- [60] P. Virtanen, R. Gommers, T. E. Oliphant, M. Haberland, T. Reddy, D. Cournapeau, E. Burovski, P. Peterson, W. Weckesser, and J. Bright, SciPy 1.0: Fundamental algorithms for scientific computing in python, *Nat. Methods* **17**, 261 (2020).
- [61] W. B. Nurdin and K.-D. Schotte, Dynamical temperature for spin systems, *Phys. Rev. E* **61**, 3579 (2000).
- [62] J. H. Mentink, M. V. Tretyakov, A. Fasolino, M. I. Katsnelson, and T. Rasing, Stable and fast semi-implicit integration of the stochastic Landau–Lifshitz equation, *J. Phys.: Condens. Matter* **22**, 176001 (2010).
- [63] N. Grønbech-Jensen and O. Farago, A simple and effective verlet-type algorithm for simulating Langevin dynamics, *Mol. Phys.* **111**, 983 (2013).
- [64] D. Wang, J. Weerasinghe, and L. Bellaiche, Atomistic molecular dynamic simulations of multiferroics, *Phys. Rev. Lett.* **109**, 067203 (2012).
- [65] G. F. Dionne, *Magnetic Oxides* (Springer, New York, 2009).
- [66] H. Dammak, Y. Chalopin, M. Laroche, M. Hayoun, and J.-J. Greffet, Quantum thermal bath for molecular dynamics simulation, *Phys. Rev. Lett.* **103**, 190601 (2009).
- [67] C. H. Woo, H. Wen, A. A. Semenov, S. L. Dudarev, and P.-W. Ma, Quantum heat bath for spin-lattice dynamics, *Phys. Rev. B* **91**, 104306 (2015).
- [68] L. Bergqvist and A. Bergman, Realistic finite temperature simulations of magnetic systems using quantum statistics, *Phys. Rev. Mater.* **2**, 013802 (2018).
- [69] K. P. Sinha and U. N. Upadhyaya, Phonon-magnon interaction in magnetic crystals, *Phys. Rev.* **127**, 432 (1962).
- [70] U. N. Upadhyaya and K. P. Sinha, Phonon-magnon interaction in magnetic crystals. II. Antiferromagnetic systems, *Phys. Rev.* **130**, 939 (1963).
- [71] P. E. Blöchl, Projector augmented-wave method, *Phys. Rev. B* **50**, 17953 (1994).
- [72] J. P. Perdew, A. Ruzsinszky, G. I. Csonka, O. A. Vydrov, G. E. Scuseria, L. A. Constantin, X. Zhou, and K. Burke, Restoring the density-gradient expansion for exchange in solids and surfaces, *Phys. Rev. Lett.* **100**, 136406 (2008).
- [73] S. L. Dudarev, G. A. Botton, S. Y. Savrasov, C. J. Humphreys, and A. P. Sutton, Electron-energy-loss spectra and the structural stability of nickel oxide: An LSDA + U study, *Phys. Rev. B* **57**, 1505 (1998).
- [74] J. H. P. Colpa, Diagonalization of the quadratic boson Hamiltonian, *Physica A* **93**, 327 (1978).
- [75] S. Toth and B. Lake, Linear spin wave theory for single-Q incommensurate magnetic structures, *J. Phys.: Condens. Matter* **27**, 166002 (2015).
- [76] See Supplemental Material at <http://link.aps.org/supplemental/10.1103/PhysRevB.109.094429> for the estimation method of uncertainties, the magnon spectrum of YIG, the spin-lattice coupling constants in three studied compounds, the assessment of SOC effects on our proposed scheme, and the evaluation of  $\alpha(q = 0)$  using the approach described in Ref. [35].
- [77] O. I. Gorbatov, G. Johansson, A. Jakobsson, S. Mankovsky, H. Ebert, I. Di Marco, J. Minár, and C. Etz, Magnetic exchange interactions in yttrium iron garnet: A fully relativistic first-principles investigation, *Phys. Rev. B* **104**, 174401 (2021).
- [78] A. J. Princep, R. A. Ewings, S. Ward, S. Tóth, C. Dubs, D. Prabhakaran, and A. T. Boothroyd, The full magnon spectrum of yttrium iron garnet, *npj Quantum Mater.* **2**, 63 (2017).
- [79] Y. Sun, Y.-Y. Song, H. Chang, M. Kabatek, M. Jantz, W. Schneider, M. Wu, H. Schultheiss, and A. Hoffmann, Growth and ferromagnetic resonance properties of nanometer-thick yttrium iron garnet films, *Appl. Phys. Lett.* **101**, 152405 (2012).
- [80] M. Onbasli, A. Kehlberger, D. H. Kim, G. Jakob, M. Kläui, A. V. Chumak, B. Hillebrands, and C. A. Ross, Pulsed laser deposition of epitaxial yttrium iron garnet films with low Gilbert damping and bulk-like magnetization, *APL Mater.* **2**, 106102 (2014).
- [81] C. Dubs, O. Surzhenko, R. Linke, A. Danilewsky, U. Brückner, and J. Dellith, Sub-micrometer yttrium iron garnet LPE films with low ferromagnetic resonance losses, *J. Phys. D: Appl. Phys.* **50**, 204005 (2017).
- [82] P. Röschmann and W. Tolksdorf, Epitaxial growth and annealing control of FMR properties of thick homogeneous Ga substituted yttrium iron garnet films, *Mater. Res. Bull.* **18**, 449 (1983).
- [83] J. Goodenough, W. Gräper, F. Holtzberg, D. Huber, R. Lefever, J. Longo, T. McGuire, and S. Methfessel, *Magnetic and Other Properties of Oxides and Related Compounds* (Springer, New York, 1970).
- [84] J.-R. Huang and C. Cheng, Cation and magnetic orders in  $\text{MnFe}_2\text{O}_4$  from density functional calculations, *J. Appl. Phys.* **113**, 033912 (2013).
- [85] P. V. Reddy, K. Pratap, and T. S. Rao, Electrical conductivity of some mixed ferrites at curie point, *Cryst. Res. Technol.* **22**, 977 (1987).
- [86] N. Hedrich, K. Wagner, O. V. Pylypovskiy, B. J. Shields, T. Kosub, D. D. Sheka, D. Makarov, and P. Maletinsky, Nanoscale mechanics of antiferromagnetic domain walls, *Nat. Phys.* **17**, 574 (2021).
- [87] W.-Z. Xiao, Y.-W. Zhang, L.-L. Wang, and C.-P. Cheng, New-type two-dimensional  $\text{Cr}_2\text{O}_3$  monolayer with half-metallicity, high Curie temperature, and magnetic anisotropy, *J. Magn. Magn. Mater.* **543**, 168657 (2022).
- [88] P. Makushko, T. Kosub, O. V. Pylypovskiy, N. Hedrich, J. Li, A. Pashkin, S. Avdoshenko, R. Hübner, F. Ganss, D. Wolf

- et al.*, Flexomagnetism and vertically graded Néel temperature of antiferromagnetic Cr<sub>2</sub>O<sub>3</sub> thin films, [Nat. Commun. \*\*13\*\*, 6745 \(2022\)](#).
- [89] S. Shi, A. L. Wysocki, and K. D. Belashchenko, Magnetism of chromia from first-principles calculations, [Phys. Rev. B \*\*79\*\*, 104404 \(2009\)](#).
- [90] A. I. Liechtenstein, V. I. Anisimov, and J. Zaanen, Density-functional theory and strong interactions: Orbital ordering in Mott-Hubbard insulators, [Phys. Rev. B \*\*52\*\*, R5467 \(1995\)](#).
- [91] C. A. Brown, Magneto-electric domains in single crystal chromium oxide, Ph.D. thesis, Imperial College London, 1969.
- [92] K. D. Belashchenko, O. Tchernyshyov, A. A. Kovalev, and O. A. Tretiakov, Magnetoelectric domain wall dynamics and its implications for magnetoelectric memory, [Appl. Phys. Lett. \*\*108\*\*, 132403 \(2016\)](#).
- [93] J. Li, J. Feng, P. Wang, E. Kan, and H. Xiang, Nature of spin-lattice coupling in two-dimensional CrI<sub>3</sub> and CrGeTe<sub>3</sub>, [Sci. China Phys., Mech. Astron. \*\*64\*\*, 286811 \(2021\)](#).